magnetochemistry

MDPI

Article

Elaboration of Luminescent and Magnetic Hybrid Networks Based on Lanthanide Ions and Imidazolium Dicarboxylate Salts: Influence of the Synthesis Conditions

Pierre Farger, Cédric Leuvrey, Mathieu Gallart, Pierre Gilliot, Guillaume Rogez, Pierre Rabu * and Emilie Delahaye *

Institut de Physique et Chimie des Matériaux de Strasbourg, Université de Strasbourg, CNRS UMR 7504, F-67034 Strasbourg CEDEX 2, France; pierre.farger@ipcms.unistra.fr (P.F.); cedric.leuvrey@ipcms.unistra.fr (C.L.); mathieu.gallart@ipcms.unistra.fr (M.G.); pierre.gilliot@ipcms.unistra.fr (P.G.); guillaume.rogez@ipcms.unistra.fr (G.R.)

* Correspondence: pierre.rabu@ipcms.unistra.fr (P.R.); emilie.delahaye@ipcms.unistra.fr (E.D.); Tel.: +33-3-8810-7130 (P.R. & E.D.); Fax: +33-3-8810-7247 (P.R. & E.D.)

Academic Editor: Kevin Bernot
Received: 7 November 2016; Accepted: 13 December 2016; Published: 22 December 2016

Abstract: The syntheses and characterization of four new hybrid coordination networks based on lanthanide ions (Ln = Nd, Sm) and 1,3-carboxymethylimidazolium (**L**) salt in the presence of oxalic acid (H_2ox) are reported. The influence of the synthesis parameters, such as the nature of the lanthanide ion (Nd^{3+} or Sm^{3+}), the nature of the imidazolium source (chloride [H_2**L**][Cl] or zwitterionic [H**L**] form) and the presence or not of oxalic acid (H_2ox), is discussed. In the presence of oxalic acid, the samarium salt gives only one compound [Sm(**L**)(ox)(H_2O)]·H_2O, whatever the nature of the imidazolium ligand, while the neodymium salt leads to three different compounds, [Nd(**L**)(ox)(H_2O)]·H_2O, [Nd(**L**)$(ox)_{0.5}$(H_2O)$_2$][Cl] or [Nd_2(**L**)$_2$(ox)(NO_3)(H_2O)$_3$][NO_3], depending on the imidazolium ligand. In the absence of oxalic acid, gels are obtained, except for the reaction between the neodymium salt and [H_2**L**][Cl], which leads to [Nd(**L**)(ox)(H_2O)]·H_2O. All compounds crystallized and their structures were determined by single crystal diffraction. The description of these new phases was consistently supported by ancillary techniques, such as powder X-ray diffraction, thermal analyses and UV-visible-near infrared spectroscopy. The luminescent and magnetic properties of the three pure compounds [Sm(**L**)(ox)(H_2O)]·H_2O, [Nd(**L**)(ox)(H_2O)]·H_2O and [Nd_2(**L**)$_2$(ox)(NO_3)(H_2O)$_3$][NO_3] were also studied.

Keywords: hybrid coordination networks; lanthanide ions; luminescence; magnetic properties

1. Introduction

Hybrid coordination polymers have been the subject of intense research for a few decades. Primarily investigated for their porosity and related properties, coordination polymers are promising for many applications, like gas separation and storage, catalysis or drug delivery, for example [1–5]. The versatility of the synthesis of such metal coordination polymers is now exploited to generate new functional hybrid networks with specific electronic properties (luminescence, magnetism, conductivity, etc.) [6–10].

Compared to the first row transition metals, the coordination number of 4f elements is more diverse. Even if a wide range of coordination numbers for lanthanides can make the prediction and control of the final structure of the networks difficult, it can be an advantage for the generation of (multi)functional systems. This (multi)functionality stems essentially from the intrinsic physical

properties of the lanthanide ions. Especially due to luminescent properties, lanthanide-based compounds can be used in many potential applications, such as light-emitting devices, sensing, imaging agents in the biomedical area, as well as solar energy conversion [11–16]. Among the different networks based on lanthanides, those containing Tb^{3+} and Eu^{3+} ions are certainly the most studied since they exhibit a characteristic green and red emission, respectively [17,18]. Moreover, lanthanide ions present a strong magnetic anisotropy, which confers them interesting magnetic properties, such as single molecule magnet or single chain magnet behavior [19–21].

The synthesis of hybrid coordination networks is very versatile since different parameters, such as the solvent, the temperature, the pH, the nature and the concentration of the reactants, can have a great influence on the final product [1,22]. Recently, the synthesis of hybrid coordination networks has been realized in ionic liquid media, which is called ionothermal synthesis. The use of ionic liquids (belonging to the family of the imidazolium or ammonium salts, for example) allows obtaining new compounds that are only available in these kinds of conditions [23–25]. However, real control of ionothermal synthesis is still limited, especially because the role of ionic liquids, acting as a solvent, structuring agent or charge compensator, or even a combination of these three possibilities, is rather unpredictable. To circumvent this problem, we have chosen to design imidazolium salts functionalized by carboxylate functions to force the role of the imidazolium salts to that of the ligand. Such a method has already proven its efficiency to get hybrid networks [26–30].

We have recently reported the synthesis of two isostructural hybrid coordination networks based on transition metal ions (M = Co^{2+}, Zn^{2+}) [31] and a series of uranyl hybrid coordination networks [32] in the presence of the imidazolium dicarboxylate salt named 1,3-bis(carboxymethyl)imidazolium chloride or [H_2**L**][Cl]. To go further into the exploration and the understanding of such a system, we analyzed the behavior of the lanthanide ions, and in particular, we investigated the behavior of the Nd^{3+} and Sm^{3+} ions.

In this paper, we report the effect of the nature of the imidazolium salt (either [H_2**L**][Cl] or 2-(1-(carboxymethyl)-1H-imidazol-3-ium-3-yl)acetate denoted [H**L**]) on the structure of lanthanide-based compounds obtained by the reaction with $Nd(NO_3)_3{\cdot}6H_2O$ or $Sm(NO_3)_3{\cdot}6H_2O$ in the presence of oxalic acid (H_2ox) in a water/ethanol mixture. The effect of the presence of oxalic acid is also investigated.

2. Results and Discussion

2.1. Crystal Structure of [Ln(L)(ox)(H_2O)]·H_2O with Ln = Nd^{3+} or Sm^{3+}

The diffraction analysis reveals that the compounds [Nd(**L**)(ox)(H_2O)]·H_2O and [Sm(**L**)(ox)(H_2O)]·H_2O are isostructural (see Table 1 and Figure S1). Consequently, only the structure of [Nd(**L**)(ox)(H_2O)]·H_2O will be described below. [Nd(**L**)(ox)(H_2O)]·H_2O crystallizes in the triclinic space group *P*-1 (No. 2) with the parameters a = 8.010(3) Å, b = 9.203(3) Å, c = 9.523(2) Å, α = 79.910(20)°, β = 72.043(16)° and γ = 89.270(20)°.

Table 1. Crystal data and structure refinement for [Sm(**L**)(ox)(H_2O)]·H_2O, [Nd(**L**)(ox)(H_2O)]·H_2O, [Nd_2(**L**)$_2$(ox)(NO_3)(H_2O)$_3$][NO_3] and [Nd(**L**)(ox)$_{0.5}$(H_2O)$_2$][Cl].

Compound	**[Sm(L)(ox)(H_2O)]·H_2O**	**[Nd(L)(ox)(H_2O)]·H_2O**	**[Nd_2(L)$_2$(ox)(NO_3)(H_2O)$_3$][NO_3]**	**[Nd(L)(ox)$_{0.5}$(H_2O)$_2$][Cl]**
Formula	$C_9H_7N_2O_{10}Sm$	$C_9H_7N_2O_{10}Nd$	$C_{16}H_{14}N_6O_{21}Nd_2$	$C_8H_7N_2O_8Cl_1Nd$
Crystal size (mm^3)	0.156 × 0.108 × 0.094	0.131 × 0.056 × 0.052	0.084 × 0.048 × 0.047	0.132 × 0.082 × 0.054
Formula weight ($g \cdot mol^{-1}$)	453.52	447.41	914.81	451.68
Temperature (K)	293(2)	293(2)	293(2)	293(2)
Wavelength (Å)	0.71073	0.71073	0.71073	0.71073
Crystal system	Triclinic	Triclinic	Triclinic	Triclinic
Space group	*P*-1	*P*-1	*P*-1	*P*-1
Unit cell dimension				
a (Å)	7.9948(9)	8.010(3)	8.076(3)	7.9870(10)
b (Å)	9.2408(15)	9.203(3)	12.545(4)	8.534(3)
c (Å)	9.434(2)	9.5230(19)	15.713(3)	11.259(3)
α (°)	80.411(13)	79.91(2)	71.896(18)	71.961(17)
β (°)	71.829(11)	72.043(16)	82.14(2)	84.27(2)
γ (°)	89.793(10)	89.27(2)	75.62(3)	68.045(18)
V ($Å^3$)	652.1(2)	656.8(3)	1462.7(8)	676.7(3)
Z	2	2	2	2
D_{calc} ($g \cdot cm^{-3}$)	2.310	2.262	2.077	2.154
Absorption coefficient (mm^{-1})	4.345	3.981	3.585	4.040
F (0 0 0)	434	430	880	420
Index range	$-9 < h < 10$ $-11 < k < 12$ $-12 < l < 11$	$-10 < h < 6$ $-11 < k < 11$ $-12 < l < 11$	$-7 < h < 10$ $-13 < k < 16$ $-17 < l < 20$	$-10 < h < 10$ $-11 < k < 9$ $-14 < l < 14$
Collected reflections	6075	6785	15481	6346
Independent reflections (Rint)	2983 (0.0382)	3005 (0.0518)	6677 (0.0840)	3091 (0.1740)
Observed reflections ($I > 2\sigma(I)$)	2662	2725	3882	2334
Refinement method	Full matrix least square on F_2	Full matrix least square on F_2	Full matrix least square on F_2	Full matrix least square on F_2
Final R indices ($I > 2\sigma(I)$)	*R*1 = 0.0297, *wR*2 = 0.0632	*R*1 = 0.0289, *wR*2 = 0.0667	*R*1 = 0.0699, *wR*2 = 0.1366	*R*1 = 0.0802, *wR*2 = 0.1828
Final R indices (all data)	*R*1 = 0.0387, *wR*2 = 0.0674	*R*1 = 0.0352, *wR*2 = 0.0697	*R*1 = 0.1517, *wR*2 = 0.1665	*R*1 = 0.1134, *wR*2 = 0.2089
S	1.087	1.074	1.051	1.076
$(Dr)_{max,\ min}$ ($e \cdot Å^{-3}$)	1.436, −1.546	0.985, −1.643	4.237, −1.229	2.860, −3.995

In the refined model, the asymmetric unit (Figure 1) contains one Nd^{3+} cation, one fully-deprotonated L^- ligand, two half oxalate ligands, one coordinated water molecule and one non-coordinated water molecule distributed on two positions (O10A and O10B) with the occupancy rates of 0.54 and 0.46, respectively.

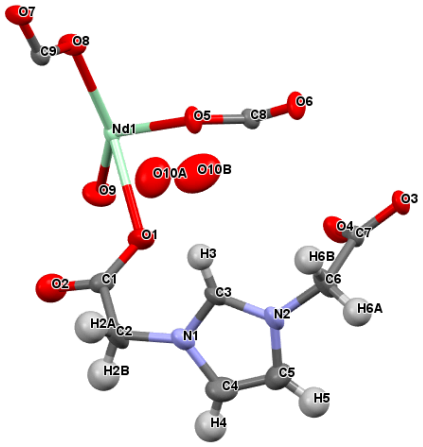

Figure 1. Ellipsoid view of the asymmetric unit of $[Nd(L)(ox)(H_2O)]\cdot H_2O$ (red: oxygen; grey: carbon; blue: nitrogen; H: hydrogen; and green: neodymium).

In the network, Nd^{3+} ions are surrounded by nine oxygens in a distorted monocapped square antiprism. Oxygen atoms belong to three different imidazolium ligands (four oxygens), two different oxalate ligands (four oxygens) and one to the coordinated water molecule. One imidazolium ligand coordinates three Nd^{3+} ions and displays a μ_3-μ_2O_3; $\kappa^2O_3O_4$; $\kappa'O_1$ coordination mode (Figure 2). One carboxylate function of the imidazolium ligand is coordinated in monodentate mode (O1). The second carboxylate function of the imidazolium ligand bridges two Nd^{3+} ions by O3 while it is coordinated to one Nd^{3+} ion with O4. The oxalate ligand coordinates two Nd^{3+} ions in bis-bidentate bridging mode as already reported [33]. These different modes of coordination give rise to dimers of lanthanide ions. These dimeric units are extended in a two-dimensional (2D) network with layers parallel to the *a*0*c* plan through oxalates with perpendicular orientation and di-oxo bridges (Figures 2 and 3a). The cavities of the network are filled by free water molecules almost equally distributed on the two different positions O10A and 10B (Figures 2 and 3b).

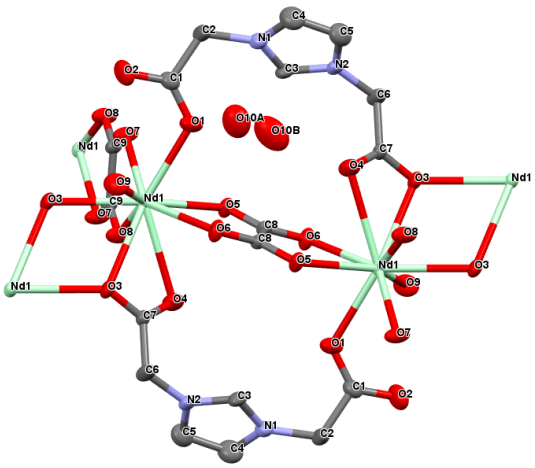

Figure 2. Selected view showing the different coordination modes in the structure of $[Nd(L)(ox)(H_2O)]\cdot H_2O$ (red: oxygen; grey: carbon; blue: nitrogen; and green: neodymium). H atoms are omitted for clarity.

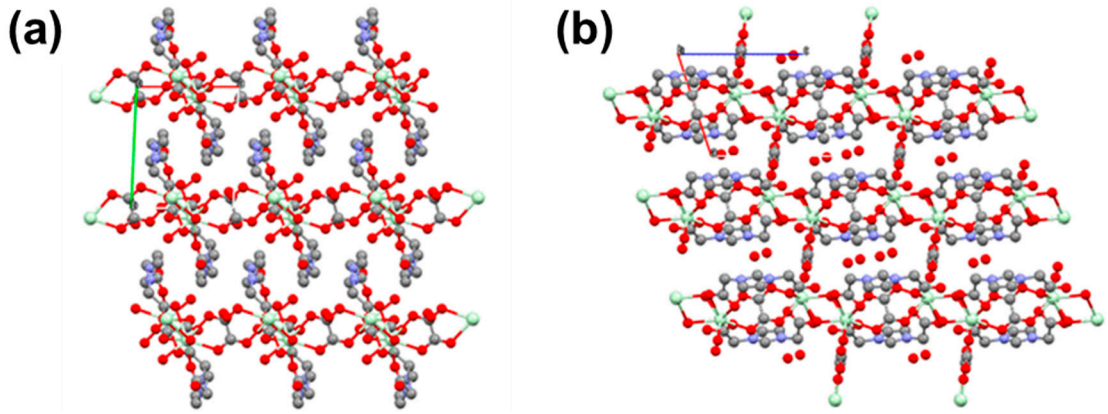

Figure 3. Selected packing view of the crystal structure of $[Nd(L)(ox)(H_2O)]\cdot H_2O$ showing: (**a**) the 2D character along the *c* axis; and (**b**) the cavities of the network along the *b* axis (red: oxygen; grey: carbon; blue: nitrogen; and green: neodymium). H atoms are omitted for clarity.

The Nd-O distances range from 2.413(3) Å to 2.731(3) Å (and from 2.385(4) to 2.716(3) Å for the compound $[Sm(\mathbf{L})(ox)(H_2O)]\cdot H_2O$). These bond lengths are comparable to those observed in similar compounds [26,34]. Nd-Nd distances are equal to 4.221(1) Å (4.189(1) Å for Sm-Sm) through the O3 di-oxo bridge and 6.285(1) Å (6.234(1) Å for Sm-Sm) through the oxalate ligand.

2.2. Crystal Structure of $[Nd_2(L)(ox)(NO_3)(H_2O)_3][NO_3]$

The compound $[Nd_2(\mathbf{L})(ox)(NO_3)(H_2O)_3][NO_3]$ is obtained as colorless crystals. It crystallizes in the triclinic space group *P*-1 (No. 2) with the parameters a = 8.076(3) Å, b = 12.545(4) Å, c = 15.713(3) Å, α = 71.896(18)°, β = 84.14(2)° and γ = 75.62(3)° (see Table 1 and Figure S1). The asymmetric unit contains two Nd^{3+} ions, two L^- ligands, two nitrate anions (one coordinated and one non-coordinated) and three coordinated water molecules (Figure 4).

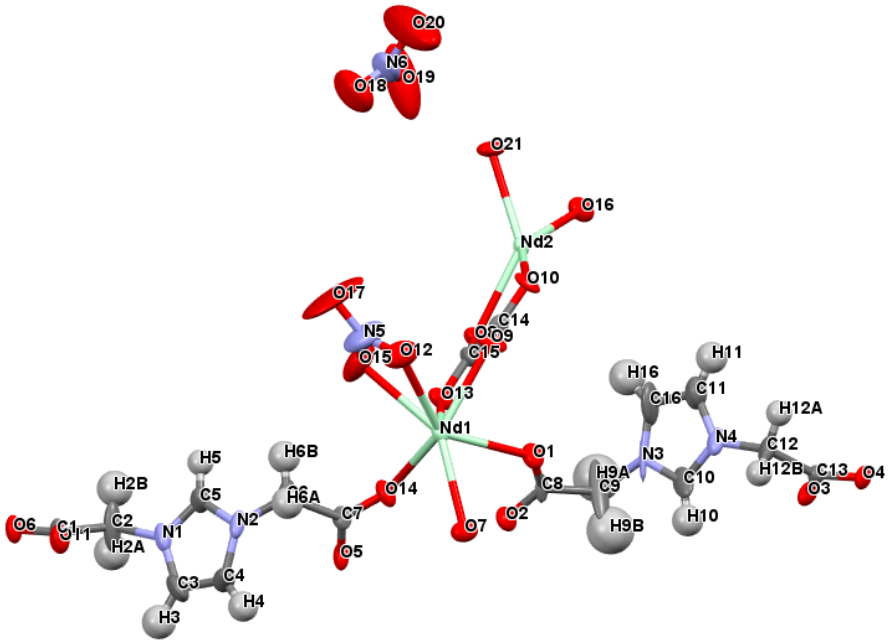

Figure 4. Ellipsoid view of the asymmetric unit of $[Nd_2(L)(ox)(NO_3)(H_2O)_3][NO_3]$ (red: oxygen; grey: carbon; blue: nitrogen, H: hydrogen; and green: neodymium).

The Nd1 ion is surrounded by nine oxygen atoms belonging to two different imidazolium ligands (O1 and O11), one oxalate ligand (O13 and O9), two coordinated water molecules (O6 and O7) and one nitrate anion (O15 and O12). The Nd2 ion is also surrounded by nine oxygen atoms belonging to three different imidazolium carboxylates (O2, O3, O4, O4 and O5), one oxalate ligand (O8 and O10) and two coordinated water molecule (O16 and O21). The two Nd^{3+} ions exhibit a tricapped trigonal prism coordination polyhedron.

The Nd1 and Nd2 ions in the asymmetric unit are connected by the oxalate ligand (O10, O8, O9 and O13) in a bis-bidentate bridging mode. The carboxylate functions (O1 and O2, O14 and O5) of two different imidazolium ligands link together asymmetric units along the *a* axis.

The Nd1 ions are linked together through the carboxylate functions (O11 and O6) of two different imidazolium ligands in a bridging bidentate mode (the Nd1–Nd1 distance is 5.20 Å), whereas the Nd2 ions are interconnected by the carboxylate functions of two other ligands (the Nd2–Nd2 distance is 10.88 Å) (Figure 5). These carboxylate functions are involved in a bidentate chelate coordination mode through O3 and O4 and in a bridging bidentate coordination mode through O4 (Figure 5).

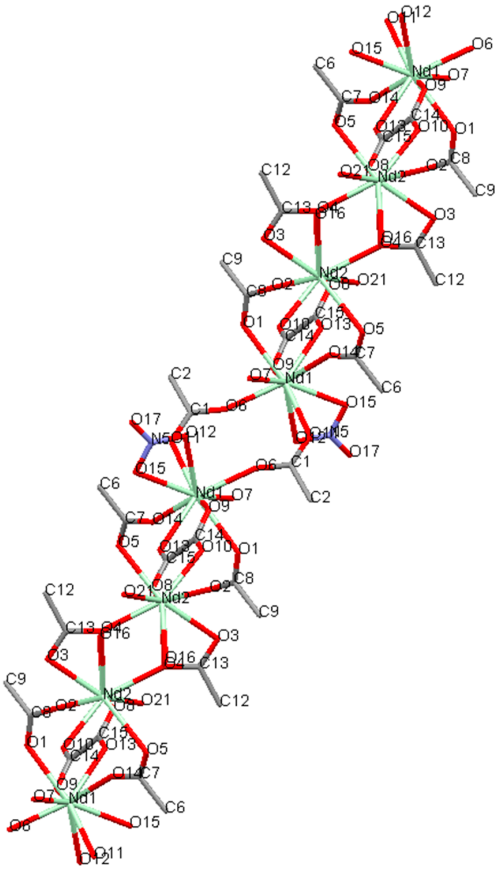

Figure 5. Selected view showing the different coordination modes for the compound $[Nd_2(\mathbf{L})(ox)(NO_3)(H_2O)_3][NO_3]$ (red: oxygen; grey: carbon; blue: nitrogen; and green: neodymium). H atoms are omitted for clarity.

As for the nitrate anions, one is coordinated to Nd1 in a bidentate chelate mode, while the second is free as previously reported for the compound $[Nd(\mathbf{L})_2(H_2O)_2][NO_3].3H_2O$ [26]. The bidentate chelate coordination mode of the nitrate anion is often reported in the literature [35,36]. Moreover, the imidazolium ligand is coordinated in a *trans* mode contrary to the previous structure $[Ln(\mathbf{L})(ox)(H_2O)]\cdot H_2O$ with Ln = Nd^{3+} or Sm^{3+} where a *cis* mode is observed. The *trans* mode gives rise to a 3D structure showing staircase linking of the Nd^{3+} ions/oxalate chains (see Figure 6). The free nitrate anions are located in the cavities of the structure. The Nd–O distances vary from

2.360(8) Å to 2.800(10) Å, and the Nd–Nd distances are equal to 4.943(2) Å and 6.413(2) Å. These distances are comparable to those observed for the previous compound [Nd(**L**)(ox)(H_2O)]·H_2O.

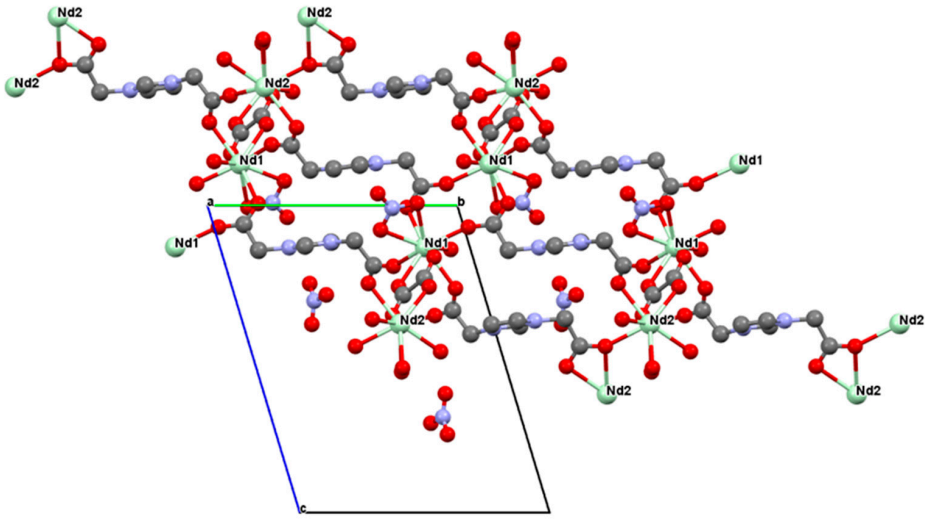

Figure 6. Selected view along the *a* axis showing different coordination modes in [Nd_2(L)(ox)(NO_3)(H_2O)$_3$] [NO_3] (red: oxygen; grey: carbon; blue: nitrogen; and green: neodymium). H atoms are omitted for clarity.

2.3. Crystal Structure of [Nd(L)(ox)$_{0.5}$(H_2O)$_2$][Cl]

The compound [Nd(**L**)(ox)$_{0.5}$(H_2O)$_2$][Cl] is obtained as colorless crystals. It crystallizes in the triclinic space group *P*-1 (No. 2) with the parameters a = 7.987(1) Å, b = 8.534(3) Å, c = 11.259(3) Å, α = 71.961(17)°, β = 84.270(20)° and γ = 68.045(18)° (see Table 1). The asymmetric unit contains one Nd^{3+} ion, one ligand L^-, one half oxalate ligand, one free chloride anion and two coordinated water molecules (Figure 7). In this structure, the Nd^{3+} ions are surrounded by nine oxygens belonging to two water molecules (O6 and O8), one oxalate ligand (O3 and O4) and three different imidazolium ligands (O1, O2, O5, $O5_{x,y,-1+z}$ and O7). The two carboxylate functions of each imidazolium ligand show different coordination modes. One carboxylate function coordinates two Nd ions through O1 and O7 in a bridging mode (O1, O7), while the second coordinates two Nd ions through O2 and O5 in a chelating bridging mode (μ_2O5; κ^2O5O2).

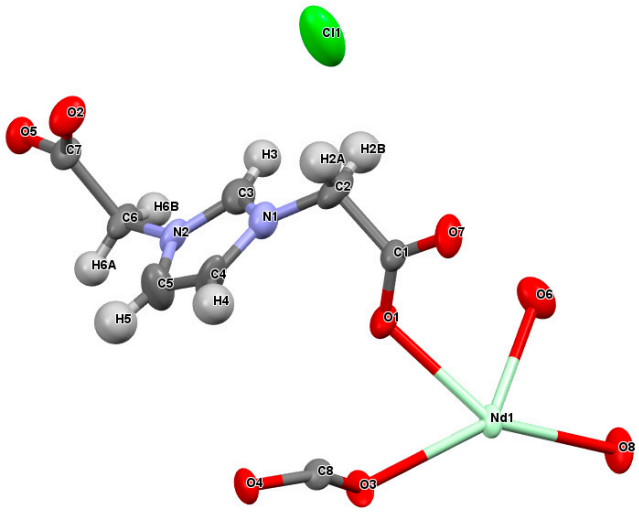

Figure 7. Asymmetric unit of [Nd(L)(ox)$_{0.5}$(H_2O)$_2$][Cl] (red: oxygen; grey: carbon; blue: nitrogen; H: hydrogen; and green: neodymium).

These different coordination modes are alternated, leading to the formation of a chain of dimeric units linked together by the oxalate ligand forming sheets parallel to the *a,b* plane. In addition, each chain is linked to another by the imidazolium ligand giving rise to a tridimensional network (Figure 8a). The chloride anion is present in the cavities of the network and is involved in hydrogen bonds with the coordinated water molecules (Figure 8b).

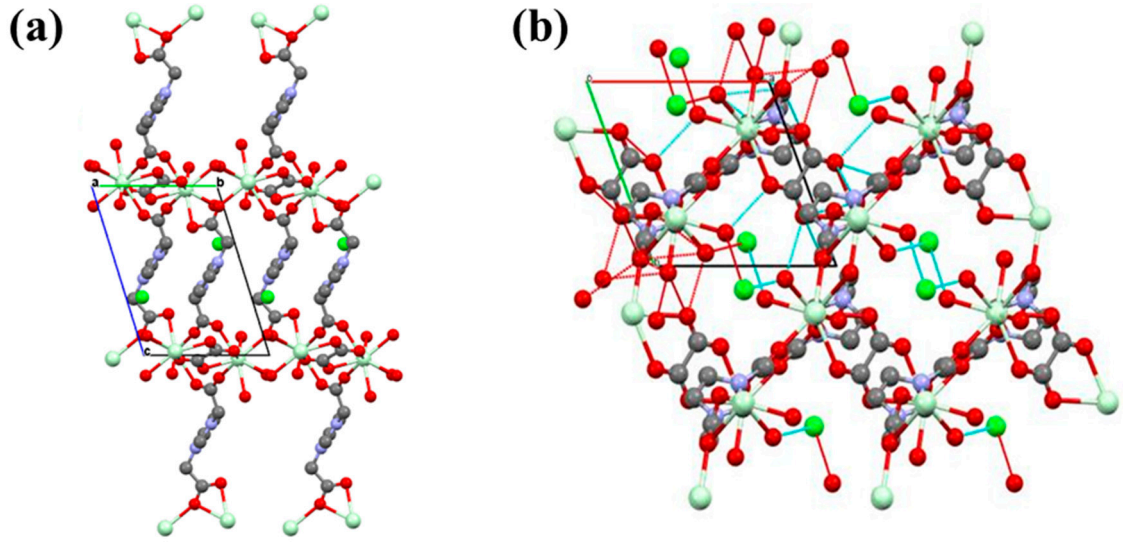

Figure 8. Selected view: (**a**) of the packing along the a axis; and (**b**) of the hydrogen bondings between the chloride anion and the networks (blue line) in $[Nd(L)(ox)_{0.5}(H_2O)_2][Cl]$ (red: oxygen; grey: carbon; blue: nitrogen; and green: neodymium). H atoms are omitted for clarity.

The Nd–O distances vary from 2.364(9) Å to 2.714(8) Å, and the Nd–Nd distances are equal to 4.987(2) Å and 6.415(2) Å through imidazolium and oxalate, respectively. These distances are similar to those observed in the previous compound $[Nd(\mathbf{L})(ox)(H_2O)]\cdot H_2O$. Though the crystalline structure was determined for the compound $[Nd(\mathbf{L})(ox)_{0.5}(H_2O)_2][Cl]$, the physical properties are not presented in the following since this compound was not obtained as a pure phase (Figure S2).

The peculiar mixed bridging-chelating coordination mode of the carboxylates encountered in both $[Nd_2(\mathbf{L})(ox)(NO_3)(H_2O)_3][NO_3]$ and $[Nd(\mathbf{L})(ox)_{0.5}(H_2O)_2][Cl]$ is reminiscent of that reported in other structures involving lanthanide ions (La^{3+} or Dy^{3+}) and linear imino diacetic acid [37]. In the latter, a "pillared" structure was observed, the ligand linking lanthanide layers; while in the present case, due to the geometry of the 1,3-carboxymethylimidazolium ligand, a staircase linking is observed between adjacent chains.

All features in the FTIR powder spectra are consistent with the single crystal structures (Figure S3) and the SEM analyses in composition mode confirm the composition of the different structures (Figure S4).

2.4. Thermal Analyses

The thermal analyses of the three compounds $[Nd_2(\mathbf{L})(ox)(NO_3)(H_2O)_3][NO_3]$, $[Nd(\mathbf{L})(ox)(H_2O)]\cdot H_2O$ and $[Sm(\mathbf{L})(ox)(H_2O)]\cdot H_2O$ are reported in Figure 9.

The thermal analysis of $[Sm(\mathbf{L})(ox)(H_2O)]\cdot H_2O$ reveals a first endothermic weight loss at 240 °C corresponding to the departure of the uncoordinated and the coordinated water molecules (calc. 7.87%; exp. 7.70%). The second weight loss observed between 300 °C and 800 °C is associated with exothermic peaks and corresponds to the decomposition of the organic species (i.e., oxalate and imidazolium ligand) and the formation of the oxide Sm_2O_3 (calc. 58.62%; exp. 57.25%). $[Nd(\mathbf{L})(ox)(H_2O)]\cdot H_2O$ shows a similar behavior. It shows a first exothermic weight loss at 190 °C corresponding to the loss of the water molecules (calc. 7.98%; exp. 8.98%) and a second one between 300 °C and 700 °C

(calc. 59.48%; exp. 57.93%) corresponding to the decomposition of the organic species and the formation of Nd_2O_3. Concerning $[Nd_2(\mathbf{L})(ox)(NO_3)(H_2O)_3][NO_3]$, the first weight loss between 35 °C and 140 °C corresponds well to the departure of nitric acid (calc. 5.87%; exp. 5.43%). This loss is immediately followed by an endothermic event between 130 °C and 240 °C, which corresponds to the departure of the two water molecules and one hydroxide (calc. 6.73%; exp. 5.94%). The successive exothermic weight losses between 200 °C and 650 °C correspond to the decomposition of the organic species (i.e., imidazolium and oxalate ligands) and the nitrate concomitant with the formation of Nd_2O_3 (calc. 50.84%; exp. 52.79%).

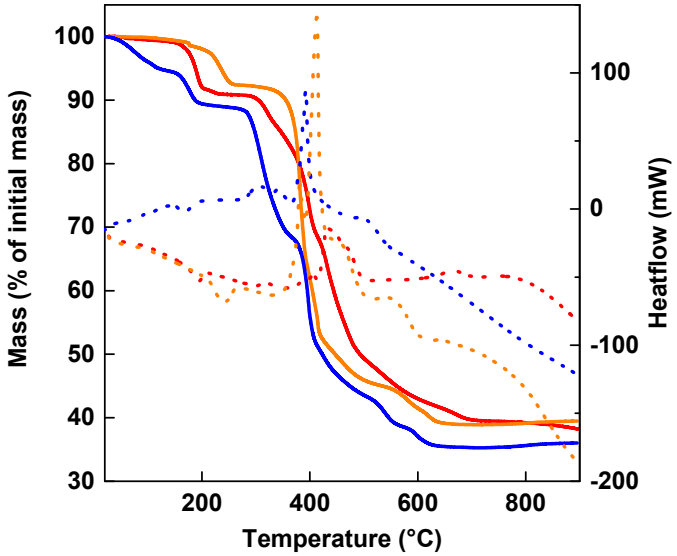

Figure 9. TGA (solid lines) and TDA (doted lines) of $[Nd_2(L)(ox)(NO_3)(H_2O)_3][NO_3]$ (blue), $[Nd(L)(ox)(H_2O)]\cdot H_2O$ (red) and $[Sm(L)(ox)(H_2O)]\cdot H_2O$ (orange).

2.5. UV-Visible-NIR Spectroscopy

The UV-visible-NIR spectra for the compounds $[Nd_2(\mathbf{L})(ox)(NO_3)(H_2O)_3][NO_3]$, $[Nd(\mathbf{L})(ox)(H_2O)]\cdot H_2O$ and $[Sm(\mathbf{L})(ox)(H_2O)]\cdot H_2O$ are displayed in Figure 10, while the assignments of the bands are reported on Table 2.

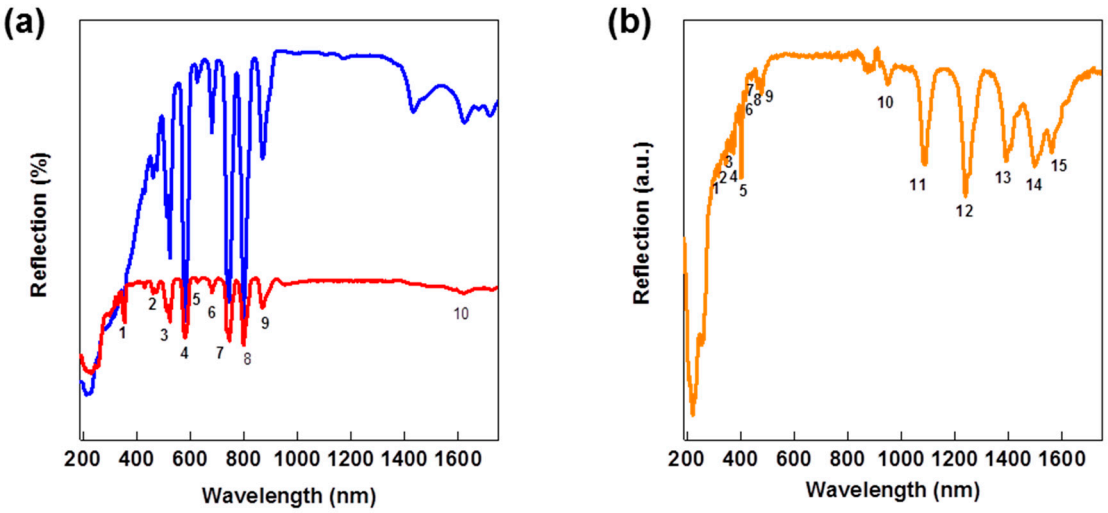

Figure 10. UV-visible-NIR spectra of the compounds: (**a**) $[Nd_2(L)(ox)(NO_3)(H_2O)_3][NO_3]$ (blue line), $[Nd(L)(ox)(H_2O)]\cdot H_2O$ (red line); and (**b**) $[Sm(L)(ox)(H_2O)]\cdot H_2O$ (orange line).

Table 2. Assignment of the bands for the compounds $[Nd_2(\mathbf{L})(ox)(NO_3)(H_2O)_3][NO_3]$, $[Nd(\mathbf{L})(ox)(H_2O)]\cdot H_2O$ and $[Sm(\mathbf{L})(ox)(H_2O)]\cdot H_2O$.

Band Number	$[Nd_2(L)(ox)(NO_3)(H_2O)_3][NO_3]$ and $[Nd(L)(ox)(H_2O)]\cdot H_2O$	$[Sm(L)(ox)(H_2O)]\cdot H_2O$
1	356 nm $^4I_{9/2}\rightarrow{}^2D_{1/2}$	318 nm $^6H_{5/2}\rightarrow{}^4F_{11/2}$
2	462 nm $^4I_{9/2}\rightarrow{}^4G_{11/2} + {}^2K_{15/2} + {}^2P_{3/2}+{}^2D_{3/2}$	344 nm $^6H_{5/2}\rightarrow{}^3H_{7/2}$
3	524 nm $^4I_{9/2}\rightarrow{}^2G_{9/2}$	362 nm $^6H_{5/2}\rightarrow{}^4F_{9/2}$
4	580 nm $^4I_{9/2}\rightarrow{}^4G_{7/2} + {}^2G_{7/2}$	376 nm $^6H_{5/2}\rightarrow{}^4D_{5/2}$
5	626 nm $^4I_{9/2}\rightarrow{}^2H_{11/2}$	404 nm $^6H_{5/2}\rightarrow{}^4K_{11/2}$
6	680 nm $^4I_{9/2}\rightarrow{}^4F_{9/2}$	418 nm $^6H_{5/2}\rightarrow{}^6P_{5/2} + {}^4M_{19/2}$
7	744 nm $^4I_{9/2}\rightarrow{}^4F_{7/2}, {}^4S_{3/2}$	440 nm $^6H_{5/2}\rightarrow{}^4G_{9/2} + {}^4I_{15/2}$
8	798 nm $^4I_{9/2}\rightarrow{}^4F_{5/2}, {}^2H_{9/2}$	464 nm $^6H_{5/2}\rightarrow{}^4F_{5/2} + {}^4I_{13/2}$
9	870 nm $^4I_{9/2}\rightarrow{}^4F_{3/2}$	478 nm $^6H_{5/2}\rightarrow{}^4I_{11/2} + {}^4M_{15/2}$
10	1624 nm $^4I_{9/2}\rightarrow{}^4I_{15/2}$	950 nm $^6H_{5/2}\rightarrow{}^6F_{11/2}$
11	-	1088 nm $^6H_{5/2}\rightarrow{}^6F_{9/2}$
12	-	1240 nm $^6H_{5/2}\rightarrow{}^6F_{7/2}$
13	-	1390 nm $^6H_{5/2}\rightarrow{}^6F_{5/2}$
14	-	1496 nm $^6H_{5/2}\rightarrow{}^6H_{15/2}$
15	-	1562 nm $^6H_{5/2}\rightarrow{}^6F_{3/2}$

The three spectra show a common band centered at 220 nm due to the intraligand π-π* transition of the imidazolium ligand [26,31,38].

The compounds $[Nd_2(\mathbf{L})(ox)(NO_3)(H_2O)_3][NO_3]$ and $[Nd(\mathbf{L})(ox)(H_2O)]\cdot H_2O$ present identical bands assigned to the transitions from the ground state $^4I_{9/2}$ to the excited states $^2D_{1/2}$, $^4G_{11/2} + {}^2K_{15/2} + {}^2P_{3/2} + {}^2D_{3/2}$, $^2G_{9/2}$, $^4G_{7/2} + {}^2G_{7/2}$, $^2H_{11/2}$, $^4F_{9/2}$, $^4F_{7/2}$, $^4S_{3/2}$, $^4F_{5/2}$, $^2H_{9/2}$, $^4F_{3/2}$ and $^4I_{15/2}$ of the Nd^{3+} ion [39,40].

The compound $[Sm(\mathbf{L})(ox)(H_2O)]\cdot H_2O$ shows also several bands assigned to transitions from the ground state $^6H_{5/2}$ to excited states $^4F_{11/2}$, $^3H_{7/2}$, $^4F_{9/2}$, $^4D_{5/2}$ $^4K_{11/2}$, $^6P_{5/2} + {}^4M_{19/2}$, $^4F_{5/2} + {}^4I_{13/2}$, $^4I_{11/2} + {}^4M_{15/2}$, $^6F_{11/2}$, $^6F_{9/2}$, $^6F_{7/2}$, $^6F_{5/2}$, $^6H_{15/2}$ and $^6F_{3/2}$ of the Sm^{3+} ion [41,42].

2.6. Luminescent Properties

The luminescent properties of $[Sm(\mathbf{L})(ox)(H_2O)]\cdot H_2O$, $[Nd(\mathbf{L})(ox)(H_2O)]\cdot H_2O$ and $[Nd_2(\mathbf{L})(ox)(NO_3)(H_2O)_3][NO_3]$ have been investigated in the solid state at room temperature.

The luminescence (excitation and emission) spectra of $[Sm(\mathbf{L})(ox)(H_2O)]\cdot H_2O$ are displayed in Figure 11. The excitation spectra (monitored for λ_{em} = 404 nm) show seven peaks corresponding to the transitions from the ground state of the Sm^{3+} ion, $^6H_{5/2}$, and excited states, $^4F_{9/2}$ (364 nm), $^4D_{5/2}$ (377 nm), $^4G_{13/2}$ (391 nm), $^4K_{11/2}$ (404 nm), $^6P_{5/2} + {}^4M_{19/2}$ (417 nm), $^4G_{9/2} + {}^4I_{15/2}$ (441 nm) and $^4F_{5/2} + {}^4I_{13/2}$ (464 nm). The emission spectra (excitation at λ_{ex} = 440 nm) show the typical band for the

Sm^{3+} ion assigned to the transition from the emitting level $^4G_{5/2}$ to $^6H_{5/2}$ (572 nm), $^6H_{7/2}$ (598 nm), $^6H_{9/2}$ (644 nm), $^6H_{11/2}$ (706 nm) and $^6F_{1/2}$ (827 nm). The transition observed at 572 nm has a magnetic dipole character [40].

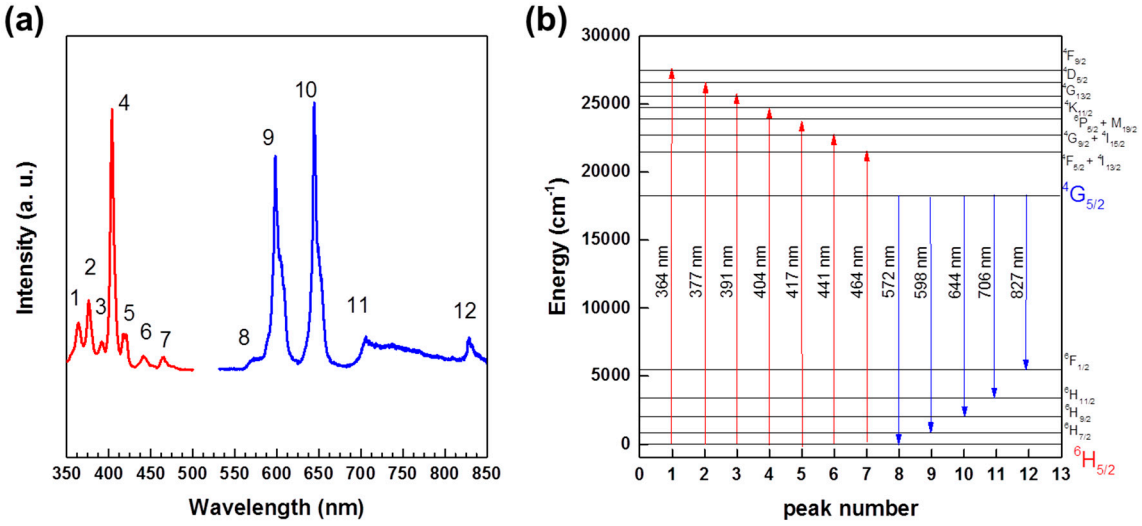

Figure 11. (**a**) Excitation spectrum (red line) and emission spectrum (blue line); and (**b**) assignment of these transitions for the compound [Sm(**L**)(ox)(H_2O)].

The emission spectra of [Nd_2(**L**)(ox)(NO_3)(H_2O)$_3$][NO_3] are displayed on Figure 12. The spectra show a broad band between 400 nm and 550 nm with a maximum at 433 nm, which is attributed to the luminescence of the imidazolium ligand [31]. The bands observed between 550 nm and 1100 nm are assigned to the transitions $^2G_{7/2} + {}^2G_{5/2} \rightarrow {}^4I_{9/2}$ (573 nm), $^2H_{11/2} \rightarrow {}^4I_{11/2}$ (620 nm), $^4S_{3/2} + {}^4F_{7/2} \rightarrow {}^4I_{11/2}$ (730 nm) and $^4F_{3/2} \rightarrow {}^4I_{9/2}$ (900 nm) and are characteristic of the Nd^{3+} ion [40,42].

The compound [Nd(**L**)(ox)(H_2O)]·H_2O does not display luminescence. This quenching of luminescence may be due to the presence of the uncoordinated water molecules in the interstitial sites, as previously reported [42,43].

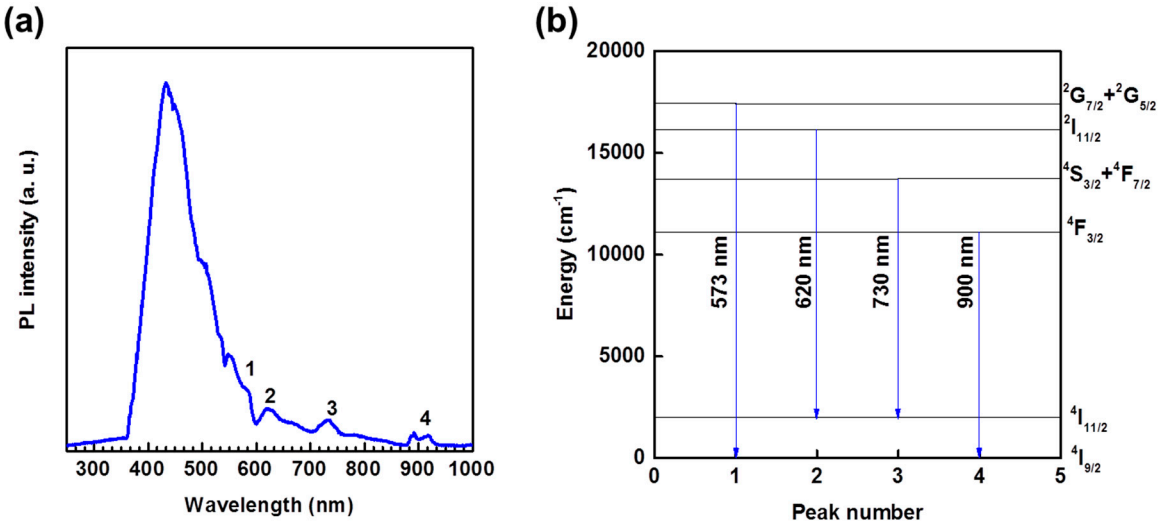

Figure 12. (**a**) Emission spectrum; and (**b**) assignment of these transitions for the compound [Nd_2(**L**)(ox)(NO_3)(H_2O)$_3$][NO_3].

2.7. Magnetic Properties

The magnetic properties of [Sm(**L**)(ox)(H_2O)]·H_2O and [Nd_2(**L**)(ox)(NO_3)(H_2O)$_3$][NO_3] were recorded under a 0.5 T DC field.

The χT product for [Sm(**L**)(ox)(H_2O)]·H_2O decreases linearly from 0.37 emu·K·mol^{-1} at 300 K to 0.02 emu·K·mol^{-1} at 1.8 K (see Figure 13). The value of the χT product at 300 K is the expected value for the isolated Sm^{3+} ion ($S = 5/2$, $g_J = 2/7$) [44]. At 52 K, the value of the χT product is equal to 0.09 emu·K·mol^{-1}, which is the theoretical value for the Sm^{3+} ion in its ground state, $^6H_{5/2}$ [45]. The value at 1.8 K is smaller, suggesting the presence of weak antiferromagnetic interactions between Sm^{3+} ions [33]. The Sm^{3+} ions exhibit strong spin-orbit coupling. To evaluate this coupling, we have fit the magnetic data by using a free ion approach for which the analytical expression of the susceptibility χ_M can be found [45]:

$$\chi_M = \frac{2.143x + 7.347 + (42.92x + 1.641)\exp(-3.5x) + (283.7x - 0.6571)\exp(-8x) + (620.6x - 1.94)\exp(-13.5x) + (1122x - 2.835)\exp(-20x) + (1813x - 3.556)\exp(-27.5x)}{3 + 4\ \exp(-3.5x) + 5\ \exp(-8x) + 6\ \exp(-13.5x) + 7\ \exp(-20x) + 8\ \exp(-27.5x)} \quad (1)$$

where λ is the spin-orbit coupling, N the Avogadro number, β the Bohr magneton, k the Boltzmann constant and $x = \lambda/kT$.

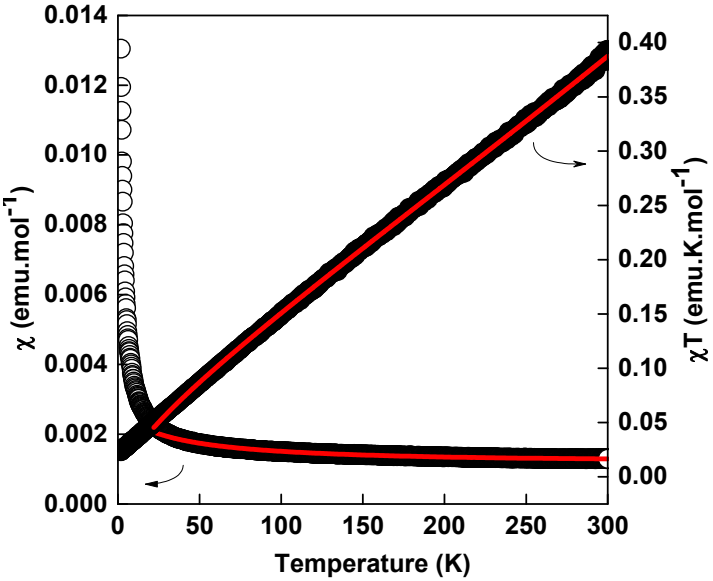

Figure 13. Plots of χ (closed circles) and χT (open circles) versus T for [Sm(**L**)(ox)(H_2O)]·H_2O. The red curves correspond to the fit of the data following the expressions mentioned in the text.

Fitting the χ vs. T curve with the above expression was not successful. We thus took into account a mean magnetic interaction between z neighboring Sm^{3+} ions zJ'. The expression of the susceptibility then becomes:

$$\chi = \frac{\chi_M}{1 - \chi_M \frac{2zJ'}{Ng_J^2\beta^2}} \quad (2)$$

where g_J is the Zeeman factor for Sm^{3+} ions. A good fit of the magnetic data was obtained between 300 K and 25 K with the best refined values λ = 256.5(2) cm^{-1} and zJ' = −4.11(3) cm^{-1}. These values are consistent with other values reported in the literature [33,44].

The spin-orbit coupling parameter allows then to determine the gap between the $^6H_{5/2}$ ground state and the first excited state $^6H_{7/2}$ of the Sm^{3+} ion. The gap is given by $E = 7\lambda/2$ = 898(1) cm^{-1} [46]. This value is consistent with the value determined by the emission spectra (760 cm^{-1}) despite the free ion approximation.

The magnetic behavior of $[Nd_2(\mathbf{L})(ox)(NO_3)(H_2O)_3][NO_3]$ is presented in Figure 14a. The χT product decreases from 1.51 emu·K·mol^{-1} at 300 K to 0.72 emu·K·mol^{-1} at 1.8 K. The magnetic behavior of $[Nd(\mathbf{L})(ox)(H_2O)]\cdot H_2O$ presented in Figure 14b is similar. The χT product decreases from 1.37 emu·K·mol^{-1} at 300 K to 0.58 emu·K·mol^{-1} at 1.8 K.

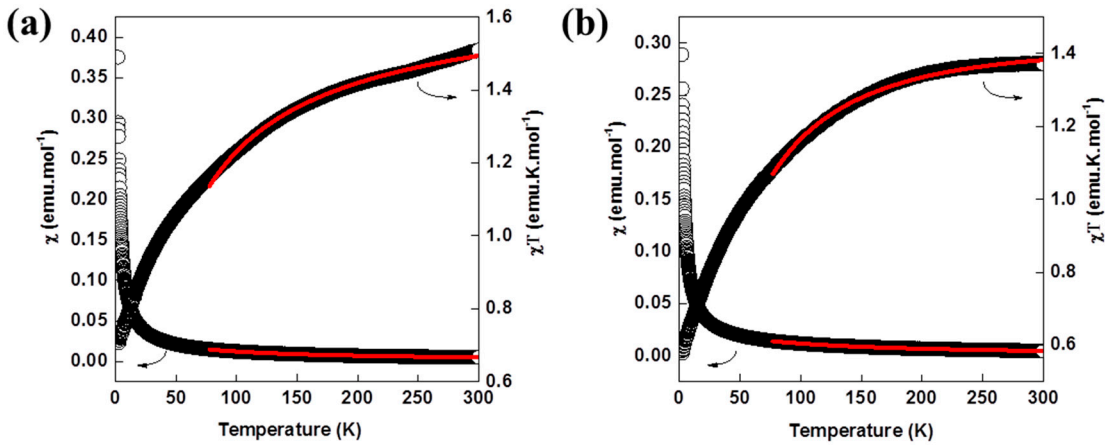

Figure 14. Plots of χ (open circles) and χT (closed circles) versus T for: (**a**) $[Nd_2(\mathbf{L})(ox)(NO_3)(H_2O)_3][NO_3]$; and (**b**) $[Nd(\mathbf{L})(ox)(H_2O)]\cdot H_2O$. The red curves represent the fit of the magnetic data.

Such behavior is commonly encountered for the isolated Nd^{3+} ion [33,47–49]. The values of the χT products at 300 K are close to that expected for the free Nd^{3+} ion (1.64 emu·K·mol^{-1} for $g_J = 8/11$). The decreasing of the χT product stems from the thermal depopulation of the low lying crystal-field states. For the Nd^{3+} ion, the first excited state is located at 2000 cm^{-1} above the ground state, and then, only the ground state is thermally populated even at 300 K. To go further, we have considered that Nd^{3+} ions may exhibit a splitting of m_j levels in an axial crystal field. The magnetic susceptibility can be described with the following expression [50]:

$$\chi = \frac{Ng^2\beta^2}{2kT} \times \frac{0.5\ \exp\left(\frac{-0.25\Delta}{kT}\right) + 4.5\ \exp\left(\frac{-2.25\Delta}{kT}\right) + 12.5\ \exp\left(\frac{-6.25\Delta}{kT}\right) + 24.5\ \exp\left(\frac{-12.25\Delta}{kT}\right) + 40.5\ \exp\left(\frac{-20.25\Delta}{kT}\right)}{\exp\left(\frac{-0.25\Delta}{kT}\right) + \exp\left(\frac{-2.25\Delta}{kT}\right) + \exp\left(\frac{-6.25\Delta}{kT}\right) + \exp\left(\frac{-12.25\Delta}{kT}\right) + \exp\left(\frac{-20.25\Delta}{kT}\right)} \quad (3)$$

where Δ is the zero field splitting parameter, N the Avogadro number, β the Bohr magneton, k the Boltzmann constant and g is the Zeeman factor for Nd^{3+} ions. The fit was performed between 75 K and 300 K (red line in Figure 14a,b), and the best refined values Δ are equal to 2.79(1) cm^{-1} and 3.06(1) cm^{-1} for $[Nd_2(\mathbf{L})(ox)(NO_3)(H_2O)_3][NO_3]$ and $[Nd(\mathbf{L})(ox)(H_2O)]\cdot H_2O$, respectively. These values are slightly higher than those encountered in the literature [33,44].

2.8. Discussion

In the case of the samarium nitrate (see Figure 15), one structure $[Sm(\mathbf{L})(ox)(H_2O)]\cdot H_2O$ is obtained when oxalic acid is added to the reaction medium whatever the nature of the imidazolium ligand (i.e., zwitterionic [H**L**] or chloride salt $[H_2\mathbf{L}][Cl]$). When the same reaction is realized without oxalic acid, the formation of a gel is observed whatever the nature of the imidazolium ligand ([H**L**] or $[H_2\mathbf{L}][Cl]$).

In the case of the neodymium nitrate (see Figure 15), the situation is slightly different and more complicated since three different structures are obtained depending on the synthesis conditions. In the presence of oxalic acid, the use of imidazolium ligand in its zwitterionic form [H**L**] leads to the formation of the pure phase $[Nd_2(\mathbf{L})(ox)(NO_3)(H_2O)_3][NO_3]$, while the use of the imidazolium ligand in its chloride form $[H_2\mathbf{L}][Cl]$ leads to a biphasic product, where the two phases have been identified as being $[Nd(\mathbf{L})(ox)(H_2O)]\cdot H_2O$ and $[Nd(\mathbf{L})(ox)_{0.5}(H_2O)_2][Cl]$. In the absence of oxalic acid, the same reaction realized with [H**L**] leads to a gel, while the use of $[H_2\mathbf{L}][Cl]$ leads to crystallized $[Nd(\mathbf{L})(ox)(H_2O)]\cdot H_2O$, which is isostructural to $[Sm(\mathbf{L})(ox)(H_2O)]\cdot H_2O$. The in situ

formation of the oxalate ligand is worth noticing here. Such an occurrence was previously reported and attributed to four possible main mechanisms: (i) the decomposition of the organic species [44,51,52]; (ii) the decarboxylation of the organic species followed by a reductive coupling of the carbon dioxide [53]; (iii) the oxidation of ethanol in the presence of nitrate anions [54]; and (iv) the hydrolysis followed by an oxidation and a decomposition of the organic species [55]. However, in the conditions used here in the presence of nitrates and alcohol, it is difficult to discuss these mechanisms further.

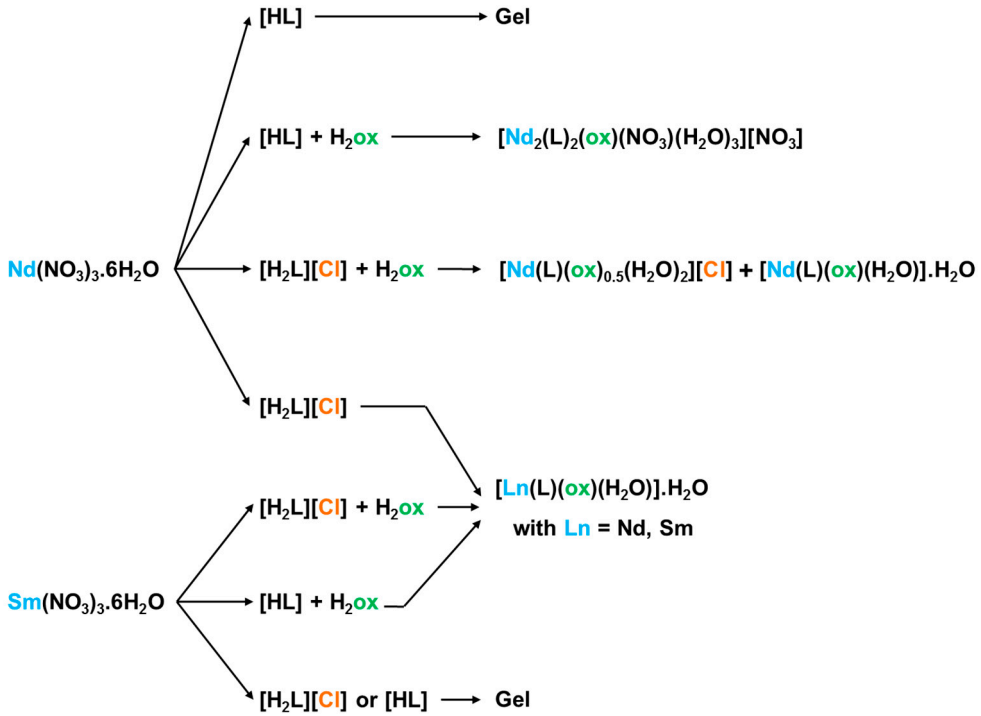

Figure 15. Recapitulative scheme indicating the compounds obtained in the water/ethanol mixture as a function of the synthesis conditions.

Nevertheless, in light of our results, it appears that the nature of the coordination networks obtained depends on three factors, which are more or less entangled: (i) the nature of the imidazolium ligand; (ii) the presence or not of oxalic acid in the parent mixture; and (iii) the nature of the lanthanide. Concerning the compounds obtained with Sm^{3+} ions, the situation is relatively simple since obtaining crystalline networks depends mainly on the presence or absence of oxalic acid. However, the situation is more complicated for the compounds obtained with Nd^{3+} ions. It is difficult to draw definitive conclusions, but it seems that the chloride anion of the imidazolium salt plays a role in the formation of the oxalate ligand and is in competition with the oxalate ligand when they are both present as starting reactants.

The modification of the obtained structures through the conditions of reaction leads for the compounds based on Nd^{3+} ions to the quenching of the luminescence properties. Indeed, in the case of [Nd(**L**)(ox)(H_2O)]·H_2O, the luminescence is quenched due to the presence of free water molecules, which is not the case with [Nd_2(**L**)(ox)(NO_3)(H_2O)$_3$][NO_3] possessing free nitrate anions. On the other hand, the magnetic behavior stays almost identical whatever the structure and is typical of isolated 4f ions with low antiferromagnetic interactions (through the oxalate ligand essentially) for the [Sm(**L**)(ox)(H_2O)]·H_2O. The value of these antiferromagnetic interactions is in the same range than those reported in the literature [33,44]. Moreover, the detailed study of the luminescence allows corroborating the approximation of free ion used in the analysis of the magnetic data.

3. Experimental Section

3.1. Materials and Methods

1-trimethylsilylimidazole, methyl chloroacetate, glycine, paraformaldehyde, glyoxal (40%) and $Nd(NO_3)_3{\cdot}6H_2O$ were purchased from Alfa Aesar (Haverhill, MA, USA) and were used as received.

Elemental analyses for C, H and N were carried out at the Service de Microanalyses of the Institut de Chimie de Strasbourg (Strasbourg, France). The SEM images were obtained with a JEOL 67000F (Tokyo, Japan) scanning electron microscope (SEM) equipped with a field emission gun (FEG), operating at 15 kV in composition mode. FTIR spectra were collected on a Perkin Elmer Spectrum Two UATR-FTIR (Waltham, MA, USA) spectrometer. UV-Vis-NIR studies were performed on a Perkin Elmer Lambda (Waltham, MA, USA) 950 spectrometer (spectra recorded in reflection mode using a 150-mm integrating sphere with a mean resolution of 2 nm and a sampling rate of 225 $nm{\cdot}min^{-1}$). TGA-TDA experiments were performed on a TA instrument SDT Q600 (New Castle, DE, USA) (heating rate of 5 $°C{\cdot}min^{-1}$ under air stream). NMR spectra in solution were recorded using a Bruker AVANCE (Billerica, MA, USA) 300 (300 MHz) spectrometer. Photoluminescence (PL) and photoluminescence excitation (PLE) measurements were performed using a broad-spectrum Energetiq® EQ-99FC (Woburn, MA, USA) laser-driven light source (LDLS™) spectrally filtered by a monochromator. The PL signal was dispersed in a spectrometer and detected by a cooled charge coupled device (CCD) camera. Magnetic measurements were performed using a Quantum Design (Quantum Design, Inc., San Diego, CA, USA) SQUID-VSM magnetometer. The static susceptibility measurements were performed in the 1.8 K–300 K temperature range with an applied field of 0.5 T. Samples were blocked in eicosane to avoid orientation under a magnetic field. Magnetization measurements at different fields and at the given temperature confirm the absence of ferromagnetic impurities. Data were corrected for the sample holder and eicosane, and diamagnetism was estimated from Pascal constants. The powder patterns were collected on a Bruker (Billerica, MA, USA) D8 diffractometer (Cu Kα = 1.540598 Å). Details for crystal data, data collection and refinement are given in Table 1. The diffraction intensities were collected with graphite-monochromatized Mo Kα radiation (λ = 0.71073 Å). Data collection and cell refinement were carried out using a Kappa Nonius (Billerica, MA, USA) CCD diffractometer at room temperature. Intensity data were corrected for Lorentz-polarization and absorption factors. The structures were solved by direct methods using SIR92 [56] and refined against F^2 by full-matrix least-squares methods using SHLEXL-2013 [57] with the anisotropic displacement parameter for all non-hydrogen atoms. All calculations were performed by using the Crystal Structure crystallographic software package WINGX [58]. The structures were drawn using Mercury [59] or Diamond. All hydrogen atoms were located on the difference Fourier map and introduced into the calculations as the riding model with isotropic thermal parameters. Crystallographic data for the structures reported have been deposited in the Cambridge Crystallographic Data Centre with CCDC reference numbers 1515568, 1515569, 1515570, 1515571 for $[Nd_2(\mathbf{L})_2(ox)(NO_3)(H_2O)_3][NO_3]$, $[Nd(\mathbf{L})(ox)_{0.5}(H_2O)][Cl]$, $[Nd(\mathbf{L})(ox)(H_2O)]{\cdot}H_2O$ and $[Sm(\mathbf{L})(ox)(H_2O)]{\cdot}H_2O$, respectively.

3.2. Synthesis

3.2.1. Synthesis of 1,3-Bis(carboxymethyl)imidazolium Chloride $[H_2\mathbf{L}][Cl]$

$[H_2\mathbf{L}][Cl]$ was synthesized as previously described [31,60].

3.2.2. Synthesis of 2-(1-(Carboxymethyl)-1H-imidazol-3-ium-3-yl)acetate [H**L**]

[H**L**] was synthesized according to the modified protocols published in the literature [61,62].

Glycine (20 mmol), glyoxal (10 mmol) and paraformaldehyde (10 mmol) were dissolved in 10 mL of water. The mixture was heated at 90 °C during 7 h. The solution was concentrated, and then, the powder was obtained with the addition of ethanol (5 mL). The brown powder was recovered by filtration and dried overnight. Yield: 65%.

Elemental analysis for [H**L**]: $C_7H_8N_2O_4$ found (calc.) (%): C 45.20 (45.65), H 4.41 (4.34), N 14.88 (15.21). ^{1}H NMR (D_2O): 4.91 (s, 4), 7.43 (d, 2), 8.76 (s, 1) ppm. ^{13}C NMR (D_2O): 50.74, 122.86, 137.20, 170.73 ppm.

3.2.3. Synthesis of $[Nd_2(\mathbf{L})_2(ox)(NO_3)(H_2O)_3][NO_3]$

[H**L**] (0.5 mmol), $Nd(NO_3)_3{\cdot}6H_2O$ (0.5 mmol) and oxalic acid (0.25 mmol) were dissolved in a 1:1 water/ethanol mixture (1.5 mL). The mixture was sealed in a Teflon-lined stainless steel bomb (6 mL) and heated at 393 K for 72 h. After cooling to room temperature, the bomb was opened, and colorless crystals were recovered by filtration and washed with ethanol. Yield: 45%.

Elemental analysis for $[Nd_2(\mathbf{L})_2(ox)(NO_3)(H_2O)_3][NO_3]{\cdot}2.9H_2O$: $C_{16}H_{25.8}N_6O_{23.9}Nd_2$ (M = 972.68 g/mol) Found (Calc.) (%): C 19.42 (19.74), H 2.53 (2.65), N 8.14 (8.63).

3.2.4. Synthesis of $[Nd(\mathbf{L})(ox)(H_2O)]{\cdot}H_2O$

$Nd(NO_3)_3{\cdot}6H_2O$ (0.5 mmol) and $[H_2\mathbf{L}][Cl]$ (0.5 mmol) were dissolved in a mixture water/ethanol (1:1 vol; 1.5 mL). The mixture was sealed in a Teflon-lined stainless bomb (6 mL) and heated at 393 K for 72 h. After cooling to room temperature, the bomb was opened, and colorless crystals were recovered by filtration and washed with ethanol (10 mL). Yield: 9.1%.

Elemental analyses: $[Nd(\mathbf{L})(ox)(H_2O)]{\cdot}2.1H_2O$: $C_9H_{13.2}N_2O_{11.1}Nd_1$ (M = 471.04 g/mol) found (calc.) (%): C 22.52 (22.93), H 2.56 (2.80), N 6.32 (5.95).

3.2.5. Synthesis of $[Nd(\mathbf{L})(ox)_{0.5}(H_2O)][Cl]$

$Nd(NO_3)_3{\cdot}6H_2O$ (0.5 mmol), oxalic acid (0.25 mmol) and $[H_2\mathbf{L}][Cl]$ (0.5 mmol) were dissolved in a mixture water/ethanol (1:1 vol; 1.5 mL). The mixture was sealed in a Teflon-lined stainless bomb (6 mL) and heated at 393 K for 72 h. After cooling to room temperature, the bomb was opened, and colorless crystals of $[Nd(L)(ox)_{0.5}(H_2O)][Cl]$ and $[Nd(L)(ox)(H_2O)]{\cdot}H_2O$ were recovered by filtration and washed with ethanol (10 mL). These two compounds are colorless and without any shape difference. It was not possible to separate the two phases. No analysis was performed on the compounds obtained during this reaction.

3.2.6. Synthesis of $[Sm(\mathbf{L})(ox)(H_2O)]{\cdot}H_2O$

$Sm(NO_3)_3{\cdot}6H_2O$ (0.5 mmol), $[H_2\mathbf{L}][Cl]$ (0.5 mmol) and oxalic acid (0.25 mmol) were dissolved in a mixture water/ethanol (1:1 vol; 1.5 mL). The mixture was sealed in a Teflon-lined stainless bomb (6 mL) and heated at 393 K for 72 h. After cooling to room temperature, the bomb was opened, and colorless crystals were recovered by filtration and washed with ethanol (10 mL). Yield: 9.1%.

Elemental analyses: $[Sm(\mathbf{L})(ox)(H_2O)]{\cdot}H_2O$: $C_9H_{11}N_2O_{10}Sm_1$ (M = 457.35 g/mol) found (calc.) (%): C 23.46 (23.61), H 2.44 (2.40), N 5.89 (6.12).

4. Conclusions

The synthesis and the characterization of four new hybrid networks based on imidazolium dicarboxylate salts and Nd^{3+} or Sm^{3+} ions have been reported. The effect of the nature of the imidazolium salts, of the lanthanide ions, as well as of the presence of oxalic acid has been highlighted for the obtained networks. For the Sm^{3+} ions, the compound $[Sm(\mathbf{L})(ox)(H_2O)]{\cdot}H_2O$ is obtained only in the presence of oxalic acid whatever the nature of the imidazolium salt. For the compounds based on Nd^{3+} ions, three different compounds can be obtained according to the reaction conditions. In the presence of oxalic acid, the chloride form of the imidazolium salt leads to a biphasic product constituted of $[Nd(\mathbf{L})(ox)_{0.5}(H_2O)][Cl]$ and $[Nd(\mathbf{L})(ox)(H_2O)]{\cdot}H_2O$, while the zwitterionic form leads to the formation of $[Nd_2(\mathbf{L})_2(ox)(NO_3)(H_2O)_3][NO_3]$. The formation of $[Nd(\mathbf{L})(ox)(H_2O)]{\cdot}H_2O$ is also observed in the absence of oxalic acid with the imidazolium salt in its chloride form. The modulation of

the obtained structures through the conditions of the reaction leads to the quenching of the luminescent properties for the Nd^{3+}-based compounds ions, while the magnetic behavior stays almost identical.

Supplementary Materials: The following are available online at www.mdpi.com/2312-7481/3/1/1/s1, Figure S1: Comparison of the calculated pattern from single crystals X-ray data (black line) and of the experimental powder X-ray diffraction patterns for the compound (a) $[Nd_2(\mathbf{L})_2(ox)(NO_3)(H_2O)_3][NO_3]$ (blue line) and (b) $[Nd(\mathbf{L})(ox)(H_2O)]\cdot H_2O$ (red line) and $[Sm(\mathbf{L})(ox)(H_2O)]\cdot H_2O$ (orange line). The green vertical lines indicate the position of the calculated diffraction lines, Figure S2: Comparison of the calculated pattern from single crystals X-ray data (black line) for $[Nd(\mathbf{L})(ox)_{0.5}(H_2O)][Cl]$ (black line) and $[Nd(\mathbf{L})(ox)(H_2O)]\cdot H_2O$ (green line) and of the experimental powder X-ray diffraction pattern (red line) of the sample coming from the reaction between $[H_2L][Cl]$, $Nd(NO_3)_3\cdot 6H_2O$ and oxalic acid, Figure S3: FTIR spectra of $[Nd_2(\mathbf{L})_2(ox)(NO_3)(H_2O)_3][NO_3]$ (blue line), $[Nd(L)(ox)(H_2O)]\cdot H_2O$ (orange line) and of $[H_2L][Cl]$ (black line) (a) on the range between 4000 cm^{-1} and 400 cm^{-1} and (b) enlargement of the range between 3500 cm^{-1} and 2500 cm^{-1}, Figure S4: SEM images in composition for the compounds (a) $[Nd_2(\mathbf{L})_2(ox)(NO_3)(H_2O)_3][NO_3]$, (b) $[Sm(L)(ox)(H_2O)]\cdot H_2O$ and (c) $[Nd(L)(ox)(H_2O)]\cdot H_2O$.

Acknowledgments: The authors thank the Centre National de la Recherche Scientifique (CNRS), the Université de Strasbourg (Idex), the Labex Nanostructures en Interaction avec leur Environnement (http://www.labex-nie.com/), the Agence Nationale de la Recherche (ANR Contract No. ANR-15-CE08-0020-01) and the Centre International de Recherche aux Frontières de la Chimie (http://www.icfrc.fr) for funding. The authors are grateful to Didier Burger (Institut de Physique et Chimie des Matériaux de Strasbourg) for technical assistance and Régis Guillot (Institut de Chimie et Matériaux Moléculaires d'Orsay) for the helpful discussions.

Author Contributions: P.F. and E.D. conceived and designed the experiments; P.F. performed the experiments; C.L. performed the SEM analysis; P.F. and E.D. performed the structural resolution, M.G. and P.G. performed the measurement of luminescence; G.R. and P.R. performed the magnetic measurements and their analysis, P.F. and E.D. wrote the paper.

Conflicts of Interest: The authors declare no conflict of interest.

References

1. Ferey, G. Hybrid porous solids: Past, present, future. *Chem. Soc. Rev.* **2008**, *37*, 191–214. [CrossRef] [PubMed]
2. Kitagawa, S.; Kitaura, R.; Noro, S.-I. Functional Porous Coordination Polymers. *Angew. Chem. Int. Ed.* **2004**, *43*, 2334–2375. [CrossRef] [PubMed]
3. Janiak, C. Engineering coordination polymers towards applications. *Dalton Trans.* **2003**, 2781–2804. [CrossRef]
4. Horcajada, P.; Serre, C.; Vallet-Regi, M.; Sebban, M.; Taulelle, F.; Ferey, G. Metal–Organic Frameworks as Efficient Materials for Drug Delivery. *Angew. Chem. Int. Ed.* **2006**, *45*, 5974. [CrossRef] [PubMed]
5. Foo, M.L.; Matsuda, R.; Kitagawa, S. Functional Hybrid Porous Coordination Polymers. *Chem. Mater.* **2014**, *26*, 310–322. [CrossRef]
6. Wang, Z.; Ananias, D.; Carné-Sánchez, A.; Brites, C.D.S.; Imaz, I.; Maspoch, D.; Rocha, J.; Carlos, L.D. Lanthanide–Organic Framework Nanothermometers Prepared by Spray-Drying. *Adv. Funct. Mater.* **2015**, *25*, 2824–2830. [CrossRef]
7. Halder, G.J.; Kepert, C.J.; Moubaraki, B.; Murray, K.S.; Cashion, J.D. Guest-Dependent Spin Crossover in a Nanoporous Molecular Framework Material. *Science* **2002**, *298*, 1762–1765. [CrossRef] [PubMed]
8. Mileo, P.G.M.; Devautour-Vinot, S.; Mouchaham, G.; Faucher, F.; Guillou, N.; Vimont, A.; Serre, C.; Maurin, G. Proton-Conducting Phenolate-Based Zr Metal–Organic Framework: A Joint Experimental–Modeling Investigation. *J. Phys. Chem. C* **2016**, *120*, 24503–24510. [CrossRef]
9. Dhara, B.; Nagarkar, S.S.; Kumar, J.; Kumar, V.; Jha, P.K.; Ghosh, S.K.; Nair, S.; Ballav, N. Increase in Electrical Conductivity of MOF to Billion-Fold upon Filling the Nanochannels with Conducting Polymer. *J. Phys. Chem. Lett.* **2016**, *7*, 2945–2950. [CrossRef] [PubMed]
10. Cirera, J. Guest effect on spin-crossover frameworks. *Rev. Inorg. Chem.* **2014**, *34*, 199–216. [CrossRef]
11. Hu, Z.; Deibert, B.J.; Li, J. Luminescent metal-organic frameworks for chemical sensing and explosive detection. *Chem. Soc. Rev.* **2014**, *43*, 5815–5840. [CrossRef] [PubMed]
12. Bunzli, J.-C.G.; Piguet, C. Taking advantage of luminescent lanthanide ions. *Chem. Soc. Rev.* **2005**, *34*, 1048–1077. [CrossRef] [PubMed]
13. Lin, R.-B.; Liu, S.-Y.; Ye, J.-W.; Li, X.-Y.; Zhang, J.-P. Photoluminescent Metal–Organic Frameworks for Gas Sensing. *Adv. Sci.* **2016**, *3*. [CrossRef] [PubMed]

14. Gándara, F.; Andrés, A.D.; Gómez-Lor, B.; Gutiérrez-Puebla, E.; Iglesias, M.; Monge, M.A.; Proserpio, D.M.; Snejko, N. A Rare-Earth MOF Series: Fascinating Structure, Efficient Light Emitters, and Promising Catalysts. *Cryst. Growth Des.* **2008**, *8*, 378–380. [CrossRef]
15. Rao, X.; Huang, Q.; Yang, X.; Cui, Y.; Yang, Y.; Wu, C.; Chen, B.; Qian, G. Color tunable and white light emitting Tb^{3+} and Eu^{3+} doped lanthanide metal-organic framework materials. *J. Mater. Chem.* **2012**, *22*, 3210–3214. [CrossRef]
16. Bünzli, J.-C.G.; Eliseeva, S.V. Lanthanide NIR luminescence for telecommunications, bioanalyses and solar energy conversion. *J. Rare Earths* **2010**, *28*, 824–842. [CrossRef]
17. Picot, A.; D'Aléo, A.; Baldeck, P.L.; Grichine, A.; Duperray, A.; Andraud, C.; Maury, O. Long-Lived Two-Photon Excited Luminescence of Water-Soluble Europium Complex: Applications in Biological Imaging Using Two-Photon Scanning Microscopy. *J. Am. Chem. Soc.* **2008**, *130*, 1532–1533. [CrossRef] [PubMed]
18. Richardson, F.S. Terbium(III) and europium(III) ions as luminescent probes and stains for biomolecular systems. *Chem. Rev.* **1982**, *82*, 541–552. [CrossRef]
19. Benelli, C.; Gatteschi, D. Magnetism of Lanthanides in Molecular Materials with Transition-Metal Ions and Organic Radicals. *Chem. Rev.* **2002**, *102*, 2369–2388. [CrossRef] [PubMed]
20. Lannes, A.; Intissar, M.; Suffren, Y.; Reber, C.; Luneau, D. Terbium(III) and Yttrium(III) Complexes with Pyridine-Substituted Nitronyl Nitroxide Radical and Different β-Diketonate Ligands. Crystal Structures and Magnetic and Luminescence Properties. *Inorg. Chem.* **2014**, *53*, 9548–9560. [CrossRef] [PubMed]
21. Bernot, K.; Bogani, L.; Caneschi, A.; Gatteschi, D.; Sessoli, R. A Family of Rare-Earth-Based Single Chain Magnets: Playing with Anisotropy. *J. Am. Chem. Soc.* **2006**, *128*, 7947–7956. [CrossRef] [PubMed]
22. Stock, N.; Biswas, S. Synthesis of Metal-Organic Frameworks (MOFs): Routes to Various MOF Topologies, Morphologies, and Composites. *Chem. Rev.* **2012**, *112*, 933–969. [CrossRef] [PubMed]
23. Reichert, W.M.; Holbrey, J.D.; Vigour, K.B.; Morgan, T.D.; Broker, G.A.; Rogers, R.D. Approaches to crystallization from ionic liquids: Complex solvents-complex results, or, a strategy for controlled formation of new supramolecular architectures? *Chem. Commun.* **2006**, 4767–4779. [CrossRef]
24. Jin, K.; Huang, X.; Pang, L.; Li, J.; Appel, A.; Wherland, S. [Cu(I)(bpp)]BF_4: The first extended coordination network prepared solvothermally in an ionic liquid solvent. *Chem. Commun.* **2002**, 2872–2873. [CrossRef]
25. Parnham, E.R.; Morris, R.E. Ionothermal Synthesis of Zeolites, Metal–Organic Frameworks, and Inorganic–Organic Hybrids. *Acc. Chem. Res.* **2007**, *40*, 1005–1013. [CrossRef] [PubMed]
26. Chai, X.-C.; Sun, Y.-Q.; Lei, R.; Chen, Y.-P.; Zhang, S.; Cao, Y.-N.; Zhang, H.-H. A Series of Lanthanide Frameworks with a Flexible Ligand, N,N′-Diacetic Acid Imidazolium, in Different Coordination Modes. *Cryst. Growth Des.* **2009**, *10*, 658–668. [CrossRef]
27. Abrahams, B.F.; Maynard-Casely, H.E.; Robson, R.; White, K.F. Copper(ii) coordination polymers of $imdc^-$ (H_2imdc^+ = the 1,3-bis(carboxymethyl)imidazolium cation): Unusual sheet interpenetration and an unexpected single crystal-to-single crystal transformation. *CrystEngComm* **2013**, *15*, 9729–9737. [CrossRef]
28. Zhang, X.-F.; Gao, S.; Huo, L.-H.; Zhao, H. A two-dimensional cobalt(II) coordination polymer: Poly[chloro(μ-imidazole-1,3-diyldiacetato-κ^4O:O′:O′′:O′′′)cobalt(II)]. *Acta Crystallogr. Sect. E* **2006**, *62*, m3359–m3361. [CrossRef]
29. Zhang, X.-F.; Gao, S.; Huo, L.-H.; Zhao, H. Poly[[chloromanganese(II)]-μ_4-imidazole-1,3-diyldiacetato]. *Acta Crystallogr. Sect. E* **2006**, *62*, m3365–m3367. [CrossRef]
30. Fei, Z.; Geldbach, T.J.; Zhao, D.; Scopelliti, R.; Dyson, P.J. A Nearly Planar Water Sheet Sandwiched between Strontium-Imidazolium Carboxylate Coordination Polymers. *Inorg. Chem.* **2005**, *44*, 5200–5202. [CrossRef] [PubMed]
31. Farger, P.; Guillot, R.; Leroux, F.; Parizel, N.; Gallart, M.; Gilliot, P.; Rogez, G.; Delahaye, E.; Rabu, P. Imidazolium Dicarboxylate Based Metal–Organic Frameworks Obtained by Solvo-Ionothermal Reaction. *Eur. J. Inorg. Chem.* **2015**, *2015*, 5342–5350. [CrossRef]
32. Martin, N.P.; Falaise, C.; Volkringer, C.; Henry, N.; Farger, P.; Falk, C.; Delahaye, E.; Rabu, P.; Loiseau, T. Hydrothermal Crystallization of Uranyl Coordination Polymers Involving an Imidazolium Dicarboxylate Ligand: Effect of pH on the Nuclearity of Uranyl-Centered Subunits. *Inorg. Chem.* **2016**, *55*, 8697–8705. [CrossRef] [PubMed]
33. Feng, X.; Ling, X.-L.; Liu, L.; Song, H.-L.; Wang, L.-Y.; Ng, S.-W.; Su, B.Y. A series of 3D lanthanide frameworks constructed from aromatic multi-carboxylate ligand: Structural diversity, luminescence and magnetic properties. *Dalton Trans.* **2013**, *42*, 10292–10303. [CrossRef] [PubMed]

34. Wang, X.-J.; Cen, Z.-M.; Ni, Q.-L.; Jiang, X.-F.; Lian, H.-C.; Gui, L.-C.; Zuo, H.-H.; Wang, Z.-Y. Synthesis Structures, and Properties of Functional 2-D Lanthanide Coordination Polymers $[Ln_2(dpa)_2(C_2O_4)_2(H_2O)_2]n$ (dpa = 2,2′-(2-methylbenzimidazolium-1,3-diyl)diacetate, $C_2O_4^{2-}$ = oxalate, Ln = Nd, Eu, Gd, Tb). *Cryst. Growth Design* **2010**, *10*, 2960–2968. [CrossRef]
35. Thuery, P. Neodymium(iii) d(−)-citramalate: A chiral three-dimensional framework with water-filled channels. *CrystEngComm* **2007**, *9*, 460–462. [CrossRef]
36. Zucchi, G.; Maury, O.; Thuéry, P.; Ephritikhine, M. Structural Diversity in Neodymium Bipyrimidine Compounds with Near Infrared Luminescence: From Mono- and Binuclear Complexes to Metal-Organic Frameworks. *Inorg. Chem.* **2008**, *47*, 10398–10406. [CrossRef] [PubMed]
37. Polido Legaria, E.; Topel, S.D.; Kessler, V.G.; Seisenbaeva, G.A. Molecular insights into the selective action of a magnetically removable complexone-grafted adsorbent. *Dalton Trans.* **2015**, *44*, 1273–1282. [CrossRef] [PubMed]
38. Wang, X.-W.; Han, L.; Cai, T.-J.; Zheng, Y.-Q.; Chen, J.-Z.; Deng, Q. A Novel Chiral Doubly Folded Interpenetrating 3D Metal-Organic Framework Based on the Flexible Zwitterionic Ligand. *Cryst. Growth Des.* **2007**, *7*, 1027–1030. [CrossRef]
39. Gabrielyan, V.T.; Kaminskii, A.A.; Li, L. Absorption and luminescence spectra and energy levels of Nd^{3+} and Er^{3+} ions in $LiNbO_3$ crystals. *Phys. Status Solidi A* **1970**, *3*, K37–K42. [CrossRef]
40. Sun, L.; Qiu, Y.; Liu, T.; Zhang, J.Z.; Dang, S.; Feng, J.; Wang, Z.; Zhang, H.; Shi, L. Near Infrared and Visible Luminescence from Xerogels Covalently Grafted with Lanthanide [Sm^{3+}, Yb^{3+}, Nd^{3+}, Er^{3+}, Pr^{3+}, Ho^{3+}] β-Diketonate Derivatives Using Visible Light Excitation. *ACS Appl. Mater. Interfaces* **2013**, *5*, 9585–9593. [CrossRef] [PubMed]
41. Li, Y.-C.; Chang, Y.-H.; Lin, Y.-F.; Chang, Y.-S.; Lin, Y.-J. Synthesis and luminescent properties of Ln^{3+} (Eu^{3+}, Sm^{3+}, Dy^{3+})-doped lanthanum aluminum germanate $LaAlGe_2O_7$ phosphors. *J. Alloys Compd.* **2007**, *439*, 367–375. [CrossRef]
42. D'Vries, R.F.; Gomez, G.E.; Hodak, J.H.; Soler-Illia, G.J.A.A.; Ellena, J. Tuning the structure, dimensionality and luminescent properties of lanthanide metal-organic frameworks under ancillary ligand influence. *Dalton Trans.* **2016**, *45*, 646–656. [CrossRef] [PubMed]
43. Hou, G.-F.; Li, H.-X.; Li, W.-Z.; Yan, P.-F.; Su, X.-H.; Li, G.-M. Two Series of Luminescent Flexible Polycarboxylate Lanthanide Coordination Complexes with Double Layer and Rectangle Metallomacrocycle Structures. *Cryst. Growth Des.* **2013**, *13*, 3374–3380. [CrossRef]
44. Cepeda, J.; Balda, R.; Beobide, G.; Castillo, O.; Fernández, J.; Luque, A.; Pérez-Yáñez, S.; Román, P. Synthetic Control to Achieve Lanthanide(III)/Pyrimidine-4,6-dicarboxylate Compounds by Preventing Oxalate Formation: Structural, Magnetic, and Luminescent Properties. *Inorg. Chem.* **2012**, *51*, 7875–7888. [CrossRef] [PubMed]
45. Andruh, M.; Bakalbassis, E.; Kahn, O.; Trombe, J.C.; Porcher, P. Structure, spectroscopic and magnetic properties of rare earth metal(III) derivatives with the 2-formyl-4-methyl-6-(*N*-(2-pyridylethyl)formimidoyl)phenol ligand. *Inorg. Chem.* **1993**, *32*, 1616–1622. [CrossRef]
46. Boča, R. *Theoretical Foundations of Molecular Magnetism*; Elsevier Science: Amsterdam, The Netherlands, 1999.
47. Lhoste, J.; Perez-Campos, A.; Henry, N.; Loiseau, T.; Rabu, P.; Abraham, F. Chain-like and dinuclear coordination polymers in lanthanide (Nd, Eu) oxochloride complexes with 2,2[prime or minute]:6[prime or minute],2[prime or minute][prime or minute]-terpyridine: Synthesis, XRD structure and magnetic properties. *Dalton Trans.* **2011**, *40*, 9136–9144. [CrossRef] [PubMed]
48. Guo, L.-R.; Tang, X.-L.; Ju, Z.-H.; Zhang, K.-M.; Jiang, H.-E.; Liu, W.-S. Lanthanide metal-organic frameworks constructed by asymmetric 2-nitrobiphenyl-4,4[prime or minute]-dicarboxylate ligand: Syntheses, structures, luminescence and magnetic investigations. *CrystEngComm* **2013**, *15*, 9020–9031. [CrossRef]
49. Manna, S.C.; Zangrando, E.; Bencini, A.; Benelli, C.; Chaudhuri, N.R. Syntheses, Crystal Structures, and Magnetic Properties of $[Ln^{III}_2(Succinate)_3(H_2O)_2]\cdot 0.5H_2O$ [Ln = Pr, Nd, Sm, Eu, Gd, and Dy] Polymeric Networks: Unusual Ferromagnetic Coupling in Gd Derivative. *Inorg. Chem.* **2006**, *45*, 9114–9122. [CrossRef] [PubMed]
50. Kahwa, I.A.; Selbin, J.; O'Connor, C.J.; Foise, J.W.; McPherson, G.L. Magnetic and luminescence characteristics of dinuclear complexes of lanthanides and a phenolic schiff base macrocyclic ligand. *Inorg. Chim. Acta* **1988**, *148*, 265–272. [CrossRef]
51. Abrahams, B.F.; Hudson, T.A.; Robson, R. Coordination networks incorporating the in situ generated ligands $[OC(CO_2)_3]^{4-}$ and $[OCH(CO_2)_2]^{3-}$. *J. Mol. Struct.* **2006**, *796*, 2–8. [CrossRef]

52. Knope, K.E.; Kimura, H.; Yasaka, Y.; Nakahara, M.; Andrews, M.B.; Cahill, C.L. Investigation of in Situ Oxalate Formation from 2,3-Pyrazinedicarboxylate under Hydrothermal Conditions Using Nuclear Magnetic Resonance Spectroscopy. *Inorg. Chem.* **2012**, *51*, 3883–3890. [CrossRef] [PubMed]
53. Mohapatra, S.; Vayasmudri, S.; Mostafa, G.; Maji, T.K. Lanthanide (LaIII/HoIII)-oxalate open framework materials formed by in situ ligand synthesis. *J. Mol. Struct.* **2009**, *932*, 123–128. [CrossRef]
54. Evans, O.R.; Lin, W. Synthesis of Zinc Oxalate Coordination Polymers via Unprecedented Oxidative Coupling of Methanol to Oxalic Acid. *Cryst. Growth Des.* **2001**, *1*, 9–11. [CrossRef]
55. Oliveira, C.K.; de Menezes Vicenti, J.R.; Burrow, R.A.; Alves, S., Jr.; Longo, R.L.; Malvestiti, I. Exploring the mechanism of in situ formation of oxalic acid for producing mixed fumarato-oxalato lanthanide (Eu, Tb and Gd) frameworks. *Inorg. Chem. Commun.* **2012**, *22*, 54–59. [CrossRef]
56. Altomare, A.; Cascarano, G.; Giacovazzo, C.; Guagliardi, A.; Burla, M.C.; Polidori, G.; Camalli, M. SIR92—A program for automatic solution of crystal structures by direct methods. *J. Appl. Crystallogr.* **1994**, *27*, 435. [CrossRef]
57. Sheldrick, G. A short history of SHELX. *Acta Crystallogr. Sect. A* **2008**, *64*, 112–122. [CrossRef] [PubMed]
58. Farrugia, L. WinGX suite for small-molecule single-crystal crystallography. *J. Appl. Crystallogr.* **1999**, *32*, 837–838. [CrossRef]
59. Edgington, P.R.; McCabe, P.; Macrae, C.F.; Pidcock, E.; Shields, G.P.; Taylor, R.; Towler, M.; van de Streek, J. Mercury: Visualization and analysis of crystal structures. *J. Appl. Crystallogr.* **2006**, *39*, 453–457.
60. Fei, Z.; Zhao, D.; Geldbach, T.J.; Scopelliti, R.; Dyson, P.J. Brønsted Acidic Ionic Liquids and Their Zwitterions: Synthesis, Characterization and pKa Determination. *Chem. A Eur. J.* **2004**, *10*, 4886–4893. [CrossRef] [PubMed]
61. VelÍŠEk, J.; DavÍDek, T.; DavÍEk, J.; TrŠKa, P.; KvasniČKa, F.; VelcovÁ, K. New Imidazoles Formed in Nonenzymatic Browning Reactions. *J. Food Sci.* **1989**, *54*, 1544–1546. [CrossRef]
62. Kühl, O.; Palm, G. Imidazolium salts from amino acids—A new route to chiral zwitterionic carbene precursors? *Tetrahedron Asymmetry* **2010**, *21*, 393–397. [CrossRef]